PCCP

PAPER

Cite this: *Phys. Chem. Chem. Phys.*, 2014, **16**, 19017

A novel model for the $(\sqrt{3} \times \sqrt{3})R30°$ alkanethiolate–Au(111) phase based on alkanethiolate–Au adatom complexes

P. Carro,*[a] X. Torrelles[b] and R. C. Salvarezza[c]

Received 24th March 2014,
Accepted 23rd July 2014

DOI: 10.1039/c4cp01255k

www.rsc.org/pccp

Self-assembled monolayers of thiols on Au(111) have attracted considerable interest from the theoretical and experimental points of view as model systems for understanding the organization of molecules on metallic surfaces, and also as key elements in nanoscience and nanotechnology. Today, there is strong theoretical and experimental evidence indicating that the surface chemistry of these monolayers at high coverage involves dithiolate–adatom (RS–Au_{ad}–SR) species, showing the existence of the (3×4) and $c(4 \times 2)$ lattices usually observed by scanning tunneling microscopy. However, concealing the existence of dithiolate–Au adatom species with the presence of the paradigmatic $(\sqrt{3} \times \sqrt{3})R30°$ lattice, which dominates the structure of long alkanethiols, still remains a challenge. Here, we propose a novel $(3\sqrt{3} \times 3\sqrt{3})R30°$ structural model containing RS–Au_{ad}–SR moieties based on DFT calculations which reconciles most of the experimental data observed for the $(\sqrt{3} \times \sqrt{3})R30°$ lattice. Our results provide a unified picture of the surface chemistry of the thiol–Au(111) system.

Introduction

Self-assembled monolayers (SAMs) of thiols are key elements in nanoscience and nanotechnology.[1] They have been widely used to link inorganic, organic and biological materials to planar gold (Au) and nanoparticle surfaces. In particular, SAMs on planar Au surfaces have been used as building blocks for the fabrication of different types of devices by the bottom-up approach with applications in biology, medicine, catalysis, photonics, and electronics.

The initial stage of thiol chemisorption on Au(111) involves the formation of lying-down phases with molecules parallel to the substrate.[2] By increasing the surface coverage, a transition from the lying-down to a standing up configuration takes place, with the formation of domains of dense and stable lattices with surface coverage $\theta = 1/3$ and nearest-neighbor thiol–thiol distances $d \approx 0.5$ nm.

The molecular backbone plays a key role in stabilizing the SAM *via* intermolecular forces ($\approx$0.1 eV per CH_2 unit) but also determines the molecular organization at the Au surface. In fact, scanning tunneling microscopy (STM) data have shown that the surface structure ranges from (3×4) for methanethiol (MT) and ethanethiol (ET)[3] to $c(4 \times 2)$ (better described as $(3 \times 2\sqrt{3})$-rect) and $(\sqrt{3} \times \sqrt{3})R30°$ lattices as the number of CH_2 units (n) in the hydrocarbon chain is increased. Moreover, STM images have revealed that domains of the $(\sqrt{3} \times \sqrt{3})R30°$ and $c(4 \times 2)$ lattices coexist on the Au surface but their relative surface coverage markedly depends on the hydrocarbon chain length. Previous results have also shown that for hexanethiol (HT) SAMs the $c(4 \times 2)$ lattice (80%) largely dominates over the $(\sqrt{3} \times \sqrt{3})R30°$ lattice (20%) while these figures are reversed for dodecanethiol (DT)[4] and hexadecanethiol (HDT).[5,6] Interestingly, STM imaging has also revealed $c(4 \times 2) \Leftrightarrow (\sqrt{3} \times \sqrt{3})R30°$ reversible transformations in domains of hexanethiol SAMs on Au(111) suggesting that both lattices have similar stability.[7]

It is well known that thiol molecules are chemisorbed on Au by strong thiolate–Au bonds ($\approx$2–3 eV). In the case of alkanethiols the chemisorption process induces a strong reconstruction of the substrate with the formation of vacancy islands (pits) of monoatomic depth on terraces. They are usually observed by STM as 2–5 nm black regions which are also covered by thiol molecules.[8] Among the different models proposed to explain the high coverage thiol lattices on the reconstructed Au(111) surface, the ones that are most widely accepted are those involving RS–Au_{ad}–SR moieties.[9] These species have been experimentally detected on the Au(111) surface by STM,[3,10] and X-ray diffraction on Au(111)[11,12] and thiol-capped Au nanoclusters[13–16], consistent with theoretical

[a] *Departamento de Química. Área Química Física, Instituto de Materiales y Nanotecnología, Universidad de La Laguna, Avda. Astrofísico Francisco Sánchez s/n, La Laguna 38071, Tenerife, Spain. E-mail: pcarro@ull.es; Tel: +34 922 318031*
[b] *Institut de Ciència de Materials de Barcelona ICMAB (CSIC), 08193 Bellaterra, Cerdanyola del Valles, Barcelona, Spain*
[c] *Instituto de Investigaciones Fisicoquímicas Teóricas y Aplicadas (INIFTA), Facultad de Ciencias Exactas, Universidad Nacional de La Plata – CONICET, Sucursal 4 Casilla de Correo 16, (1900) La Plata, Argentina*

modeling.[9,17–20] The presence of the vacancy islands on thiolate-covered Au(111) terraces has also been considered as indirect but strong experimental evidence for the presence of RS–Au_{ad}–SR moieties. In fact, these islands would result by surface diffusion, nucleation and growth of the single vacancies produced by the removal of the Au_{ad} from the Au(111) surface to form the RS–Au_{ad}–SR species. This interpretation is supported by the surface coverage of vacancy islands θ_{vac} = 0.12/0.14 measured on large Au terraces after hexanethiolate and dodecanethiolate SAM formation. In fact, this coverage is close to θ_{vac} = 1/6 as expected for RS–Au_{ad}–SR species forming a thiol lattice with θ = 1/3.[21] The RS–Au_{ad}–SR complexes are compatible with the (3 × 4) (RS–Au_{ad}–SR in *trans* configuration) and $c(4 \times 2)$ (RS–Au_{ad}–SR in *cis* configuration) surface structures with the (3 × 4) to $c(4 \times 2)$ transition for $n > 2$ explained in terms of a better hydrocarbon chain organization.[22,23] The influence of the hydrocarbon chains in stabilizing the RS–Au–SR moieties has also been analyzed.[24] In contrast, the structure of the paradigmatic $(\sqrt{3} \times \sqrt{3})R30^\circ$ lattice imaged by STM, which largely dominates for alkanethiols with $n > 10$, has remained unsolved to date.[21] In fact, present models for the $(\sqrt{3} \times \sqrt{3})R30^\circ$ surface structure involve either RS–Au_{ad} units[25] or Au vacancies[26] both with θ_{vac} = 1/3, although θ_{vac} = 0.12/0.14 has been experimentally measured (as vacancy islands) suggesting the presence of RS–Au_{ad}–SR species.[10] Also the existing models for this lattice fail to describe the $c(4 \times 2) \Leftrightarrow (\sqrt{3} \times \sqrt{3})R30^\circ$ transitions[7] since their difference in stability is very high[21] to allow reversible transitions. Finally, they also fail to explain why the $(\sqrt{3} \times \sqrt{3})R30^\circ/c(4 \times 2)$ coverage ratio increases as the hydrocarbon chain length increases.[4]

In this work the system under theoretical modeling consists of Au domains, which can be located at terraces or at the bottom of monoatomic in depth vacancy islands both covered by thiolate $c(4 \times 2)$ or $(\sqrt{3} \times \sqrt{3})R30^\circ$ lattices. This system has been extensively described in the literature as the result of thiolate adsorption on the Au(111) surface. This is an important point because our models have not single vacancies since they diffuse and coalesce to form the vacancy islands observed by STM on the Au(111) surface.

We propose a novel $(3\sqrt{3} \times 3\sqrt{3})R30^\circ$ structural model consisting of three RS–Au_{ad}–SR moieties with their S atoms in atop positions, and also other three atop thiolate adsorbed species (RS-). We have selected S atoms in atop sites since different experimental results indicate that the S–Au distance is consistent with the S atom at these sites.[27,28]

We also analyze the stability of the new model in relation with the $c(4 \times 2)$ lattice formed by RS–Au_{ad}–SR moieties as a function of the hydrocarbon chain length. The new model explains most of the experimental data reported for the $(\sqrt{3} \times \sqrt{3})R30^\circ$ lattice and thus provides for the first time a unified picture of the alkanethiol–Au(111) system in terms of surface chemistry.

Methods

Density functional calculations have been performed with the periodic plane-wave basis set code VASP 5.2.12.[29,30] We have followed the scheme of non-local functional proposed by Dion *et al.*,[31] vdW-DF, and the optimized Becke88 exchange functional optB88-vdW[32] to take into account the van der Waals (vdW) interactions. The electronic wave functions were expanded in a plane-wave basis set with a 420 eV cutoff energy. The projector augmented plane wave (PAW) method has been used to represent the atomic cores[33] with PBE potential. Gold surfaces were represented by a five atomic layer slab with ~14 Å vacuum. Optimal grids of Monkhorst-Pack[34] *k*-points of 5 × 4 × 1, 3 × 3 × 1 and 9 × 9 × 1 have been used for $c(4 \times 2)$, $(3\sqrt{3} \times 3\sqrt{3})R30^\circ$ and $(\sqrt{3} \times \sqrt{3})R30^\circ$ surface structures, respectively. Surface relaxation is allowed in the top three Au layers of the slab as well as in the atomic coordinates of the adsorbates. Alkanethiol radical species were optimized in an asymmetric box of 10 Å × 12 Å × 14 Å. The calculated lattice constant is 4.16 Å, which compares reasonably well with the experimental value (4.078 Å).[35]

The average binding energy per adsorbed species on the Au(111) surface, E_b, is defined in eqn (1):

$$E_b = \frac{1}{N_{thiol}}\left[E^{thiol/Au} - E^{R}_{Au(111)} - N_{thiol}E_{thiol}\right] \quad (1)$$

where, $E^{thiol/Au}$, $E^{R}_{Au(111)}$ and E_{thiol} stand for the total energy of the adsorbate–substrate system, the total energy of the Au slab when RS moieties are removed and the alkanethiol radical, respectively, whereas N_{thiol} is the number of alkanethiolate radicals in the surface unit cell. A negative number indicates that adsorption is exothermic with respect to the separate clean surface and alkanethiol radical.

Constant current scanning tunneling microscopy (STM) images were simulated by p4vasp software within the Tersoff–Hamann method in its most basic form with the STM tip approximated as a point source.[36]

The in-plane X-ray diffraction patterns have been simulated using the Ana-ROD software.[37]

Results and discussion

Fig. 1 shows the optimized $c(4 \times 2)$ and the $(3\sqrt{3} \times 3\sqrt{3})R30^\circ$ surface structures for HT on Au(111). Both lattices have θ = 1/3 and nearest-neighbor thiol–thiol distances $d \approx 0.5$ nm. The most important difference between these lattices is the surface coverage of RS–Au_{ad}–SR moieties which becomes 1/6 for the $c(4 \times 2)$ and 1/9 for the $(3\sqrt{3} \times 3\sqrt{3})R30^\circ$ surface structure, respectively. Note that the $(3\sqrt{3} \times 3\sqrt{3})R30^\circ$ lattice also contains a surface coverage of 1/9 of chemisorbed RS- species. On the other hand, according to the number of Au_{ad} involved θ_{vac} should be 1/6 and 1/9 for the $c(4 \times 2)$ and $(3\sqrt{3} \times 3\sqrt{3})R30^\circ$ lattices, respectively. Note that mixed RS–Au_{ad}–SR moieties and RS- species have already been considered for modeling the thiolate Au(111) interface but in the frame of $c(4 \times 2)$ surface structures[12,38]

The detailed structural information of the calculations is displayed in Table 1, where we show the tilt of the molecular axis with respect to the surface normal (α_{tilt}), the angle between the S–C_1 bond and the surface normal (α_1), the S atom–S atom distance (d(S–S)), the S–Au adatom distance (d(S–Au_{ad})), and the S-surface Au atom vertical distance (z(S–Au_{surf})). In order to

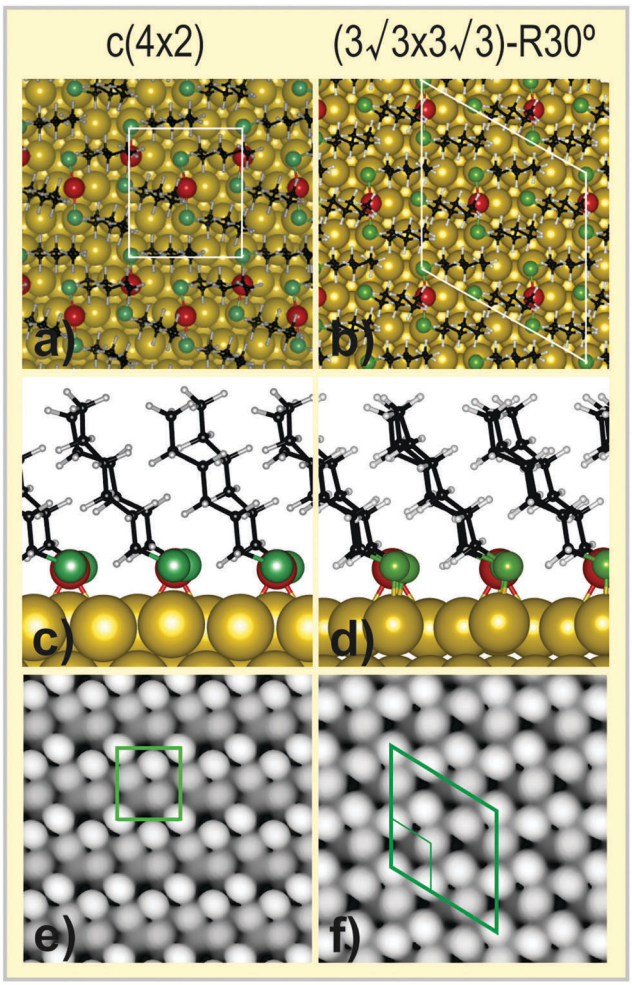

Fig. 1 (a–d) Optimized hexanethiolate surface structures on Au(111). Left panel: $c(4 \times 2)$ Right panel: $(3\sqrt{3} \times 3\sqrt{3})R30^\circ$ In (a) and (b) top view, in (c) and (d) lateral view of the surface structures. Green: S; black: C; white: H; red: Au adatom; yellow: Au. The corresponding unit cells are drawn on the figures. (e) and (f) show simulated constant current STM images of the $c(4 \times 2)$ (e) and $(3\sqrt{3} \times 3\sqrt{3})R30^\circ$ (f) lattices. The corresponding unit cells are drawn on the images. The $(\sqrt{3} \times \sqrt{3})R30^\circ$ unit cell is also included in (f).

highlight the results, all these geometrical parameters have been averaged between equivalent positions. We have found no significant differences in the structural data of these lattices, all of them being in good agreement with those experimentally reported for alkanethiol SAMs on Au(111).[21]

In particular the z(S–Au$_{surf}$) is in excellent agreement with those experimentally found for different alkanethiolate $(\sqrt{3} \times \sqrt{3})R30^\circ$ lattices on the Au(111) interface.[27]

The STM images of the optimized lattices (Fig. 1(a) and (b)) have been acquired by means of the charge density given by the DFT calculation and considering the states between 1–1.5 eV above and below the Fermi level. The simulated STM images (Fig. 1(e–f)) are in excellent agreement with those reported for the $c(4 \times 2)$ and the $(\sqrt{3} \times \sqrt{3})R30^\circ$ lattices.[21]

The E_b values of the lattices have been also included in Table 1. Our calculations show that the HT adsorption is stronger in the $c(4 \times 2)$ surface structure, as the binding energy difference ΔE_b (E_b $c(4 \times 2)$ − $E_b(3\sqrt{3} \times 3\sqrt{3})R30^\circ$) is −0.32 eV. However, as already discussed,[39] the binding energy is not a valid criterion in order to predict the stability of the different surface structures, since it does not consider the energy cost to reconstruct the Au(111) surface, *i.e.* the energy required to remove the Au adatoms needed to form the RS–Au$_{ad}$–SR moieties. Therefore, in order to estimate the stability of the $c(4 \times 2)$ and the $(3\sqrt{3} \times 3\sqrt{3})R30^\circ$ lattices shown in Fig. 1, we have compared the two energetic terms per thiol adsorbed: on one hand, the cost to form the reconstructed surface, E_{rec}/N_{thiol}, and, on the other hand, the gain of stability when one thiol binds to the surface, E_b. The reconstruction energy per unit cell (Table 1) for the different surfaces has been calculated as

$$E_{rec} = E^{R}_{Au(111)} - E^{U}_{Au(111)} - n_{ad}\, E^{Au}_{bulk} \quad (2)$$

where $E^{R}_{Au(111)}$, $E^{U}_{Au(111)}$ correspond to the energy of reconstructed Au(111) surface and unreconstructed Au(111) surface per cell unit, respectively; E^{Au}_{bulk} is the total energy of a bulk Au atom and n_{ad} is the number of Au adatoms in the surface unit cell. This energy is related to the Au adatom formation, which yields the RS–Au$_{ad}$–SR moieties. Therefore, the energetic balance per adsorbed thiol on both surface structures should be estimated as $E_b + E_{rec}/N_{thiol}$. Results from these calculations indicate that hexanethiol adsorbed on $c(4 \times 2)$ surface structure is slightly more stable than on the $(3\sqrt{3} \times 3\sqrt{3})R30^\circ$ lattice by ≈ -0.14 eV (Table 1). The relatively small difference in stability may explain not only why domains of these lattices coexist on the Au surface but also the relative surface coverage observed for HT SAMs: 80% for the $c(4 \times 2)$ and 20% for $(\sqrt{3} \times \sqrt{3})R30^\circ$ lattices observed in STM images. Moreover, this small difference is consistent with the experimentally observed reversible

Table 1 Energetic and structural data for BT, HT and OT surface structures on Au(111)

	BT		HT		OT	
Surface lattice	$(3\sqrt{3} \times 3\sqrt{3})R30^\circ$	$c(4 \times 2)$	$(3\sqrt{3} \times 3\sqrt{3})R30^\circ$	$c(4 \times 2)$	$(3\sqrt{3} \times 3\sqrt{3})R30^\circ$	$c(4 \times 2)$
E_b/eV	−2.94	−3.28	−3.17	−3.49	−3.38	−3.68
E_{rec}/N_{thiol}/eV	+0.33	+0.52	+0.34	+0.52	+0.34	+0.58
$E_b + E_{rec}/N_{thiol}$/eV	−2.61	−2.76	−2.83	−2.97	−3.04	−3.10
d(S–S)/Å	5.19	5.10	5.11	5.10	5.10	5.10
z(S–Au$_{surf}$)/Å	2.44	2.54	2.44	2.54	2.43	2.49
d(S–Au$_{ad}$)/Å	2.34	2.34	2.34	2.34	2.34	2.34
α_{tilt}/°	37.4	34.4	35.7	32.2	32.7	31.9
α_1/°	66.1	62.5	65.7	63.5	64.9	63.8

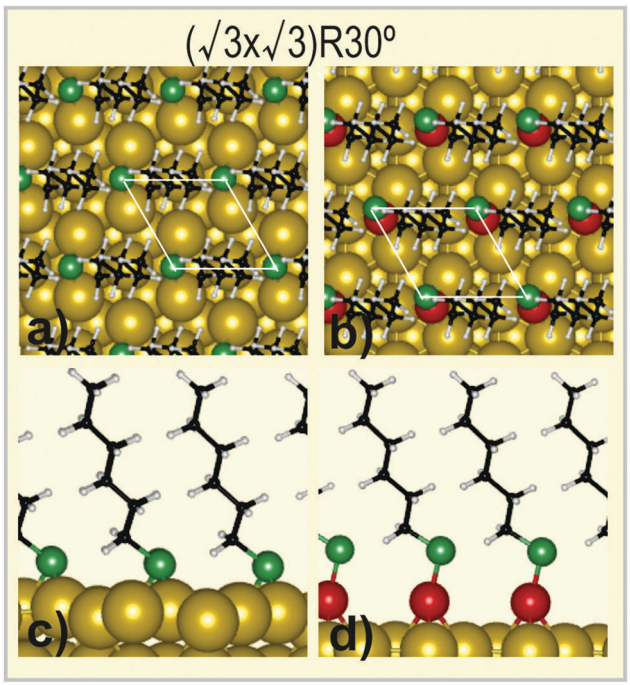

Fig. 2 (a–d) Optimized hexanethiolate $(\sqrt{3} \times \sqrt{3})R30^\circ$ surface structures on Au(111). Left panel: unreconstructed surface right panel: reconstructed surface with RS–Au_{ad} moieties. In (a) and (b) top view, in (c) and (d) lateral view of the surface structures. Green: S; black: C; white: H; red: Au adatom; yellow: Au. The corresponding unit cells are drawn on the figures.

transitions between domains of these lattices under the scanning of the STM tip.[6] We have also calculated the binding energy, E_b, of the $(\sqrt{3} \times \sqrt{3})R30^\circ$ HT lattice adsorbed at fcc-bridge sites of the unreconstructed Au(111) surface (E_r = 0) (Fig. 2a). This lattice becomes 0.19 eV more unstable ($E_b + E_{rec}/N_{thiol}$) than the HT $(3\sqrt{3} \times 3\sqrt{3})R30^\circ$ lattice suggesting that alkanethiol adsorption could induce the reconstruction of the Au(111) surface (Table 2). It can be argued that this difference is also small so that $(\sqrt{3} \times \sqrt{3})R30^\circ$ and $(3\sqrt{3} \times 3\sqrt{3})R30^\circ$ lattices can coexist on the Au surface. However, the $(3\sqrt{3} \times 3\sqrt{3})R30^\circ$ lattice is consistent with photoelectron diffraction[40] and grazing incidence X-ray diffraction[6] data indicating that S atoms are placed in atop sites rather than at the fcc-bridge sites corresponding to the $(\sqrt{3} \times \sqrt{3})R30^\circ$ lattice. Furthermore, the $(3\sqrt{3} \times 3\sqrt{3})R30^\circ$ model is in agreement with STM images of domain boundaries which had been assigned to RS–Au_{ad} species fcc hollow sites.[41] Finally, the presence of RS–Au_{ad}–SR species in the $(3\sqrt{3} \times 3\sqrt{3})$-$R30^\circ$ model explain vacancy islands

Table 2 Energetic and structural data for HT $(\sqrt{3} \times \sqrt{3})R30^\circ$ surface structures on Au(111)

	HT $(\sqrt{3} \times \sqrt{3})R30^\circ$	
Metal surface	Unreconstructed	Reconstructed[42,43]
Surface site	fcc-bridge	atop
E_b/eV	−2.64	−2.85
E_{rec}/N_{thiol}/eV	0.0	+0.76
$E_b + E_{rec}/N_{thiol}$/eV	−2.64	−2.09

formation by removal of Au_{ad} from the Au(111) surface. Obviously these features can not be explained by the fcc-bridge site model on the unreconstructed Au(111) surface.

Next we analyze other model proposed in the literature to explain the $(\sqrt{3} \times \sqrt{3})R30^\circ$ lattice. This model involves RS–Au_{ad} moieties rather than RS–Au_{ad}–SR species (Fig. 2b).[42,43] The energetic information of this lattice is shown in Table 2. It is evident by comparing the ($E_b + E_{rec}/N_{thiol}$) values that this surface model is less stable than the $(3\sqrt{3} \times 3\sqrt{3})R30^\circ$ lattice (Table 1). Also, this model needs θ_{vac} = 0.33, a figure much higher than that measured in the experimental systems.

To test the experimental plausibility of the proposed $(3\sqrt{3} \times 3\sqrt{3})R30^\circ$ lattice we calculated its X-ray diffraction pattern.[37] To proceed, it is necessary to take into account that: (i) the rotation of the $(3\sqrt{3} \times 3\sqrt{3})R30^\circ$ lattice relative to the substrate makes its surface symmetry $p31m$ rather than $p3m1$ relative to the substrate; (ii) the particular linear morphology of the thiol chains facilitates the breaking of the symmetry elements in the unit cell; (iii) the experimental intensities would reflect the symmetry of the surface cell, even if atoms/molecules present in the cell don't follow it by promoting the formation of domains related between them by the symmetry elements present in the unit cell.

The three RS–Au_{ad}–SR moieties and the three atop thiolates in Fig. 1b don't satisfy the $p31m$ symmetry of the cell; however, it is recovered when considering at least six domains, resulting from three ternary axes and three mirror planes present in the cell, to compute the theoretical diffraction pattern. Extra domains could also be considered to take into account the particular orientation of the thiol chains (azimuthal and polar angles) but were checked to have a minor relevance in the computation of the intensities. Fig. 3 shows the two-dimensional intensity distribution at the particular L-value of the non-equivalent reciprocal space quadrant. The intensities of the $(3\sqrt{3} \times 3\sqrt{3})R30^\circ$ structure are similar to those of the $(\sqrt{3} \times \sqrt{3})R30^\circ$ structure, so their intensities would have enough signal to be measured by grazing incidence X-ray diffraction techniques (GIXRD) in case the proposed model would correspond to a real surface structure.

Fig. 4 shows three fractional order rods to compare the relative intensities becoming three different fractional order rods, (H, K) = (1, 0), (1, 1) and (3, 0). The (3, 0) reflection corresponds to the average of the nine $(\sqrt{3} \times \sqrt{3})$ units forming part of the $(3\sqrt{3} \times 3\sqrt{3})R30^\circ$ model structure while the other two correspond exclusively to the $(3\sqrt{3} \times 3\sqrt{3})R30^\circ$ cell.

In the following we will discuss the stability of the different surface structures as n is increased for the $(3\sqrt{3} \times 3\sqrt{3})R30^\circ$, $c(4 \times 2)$ and the unreconstructed $(\sqrt{3} \times \sqrt{3})R30^\circ$. In this case we have used the surface free energy (γ) that can be estimated using the DFT total energies[39,44] as,

$$\gamma = \frac{N_{thiol}}{A}\left[E_b + \frac{E_{rec}}{N_{thiol}}\right] \quad (3)$$

where A is the unit cell area. Results shown in Fig. 5a for butanethiolate (BT), HT and octanethiolate (OT) clearly show that the difference in surface stability between these lattice models markedly decreases as n is increased. While for BT the

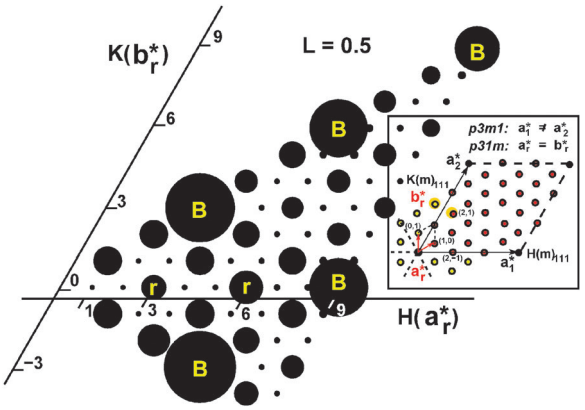

Fig. 3 Portion of the two-dimensional non-equivalent reciprocal space quadrant generated from the model of Fig. 1b using 6 symmetry *p31m* related domains. B and r characters identify the reflections having bulk/substrate or contributions from the average ($\sqrt{3} \times \sqrt{3}$) units forming part of the ($3\sqrt{3} \times 3\sqrt{3}$)*R*30° structure, respectively. The areas of the circles are proportional to the corresponding calculated structure factors. The areas of bulk circles have been reduced by a factor 3 to enhance the contrast of the smallest ones. The image shows a reciprocal space section cut at $L = 0.5$. (*H*, *K*, *L*) denote the Miller indexes expressed in reciprocal lattice units. Inset: the reciprocal space diagram showing the reciprocal lattice vectors for both the Au(111) substrate (a_1*, a_2*) and the ($3\sqrt{3} \times 3\sqrt{3}$)*R*30° superstructure ($a_r$*, b_r*). The (m) label along *H* and *K* Au(111) directions denotes mirror planes. (Red circles) Non-equivalent portion of the reciprocal space corresponding to the ($3\sqrt{3} \times 3\sqrt{3}$)*R*30° lattice where reflections of the main figure were calculated; (colored dots) fractional reflections from the ($3\sqrt{3} \times 3\sqrt{3}$)*R*30° superstructure. Reflections outlined in gold/yellow, *i.e.*, (*H*, *K*) = (2, 1) are equivalent between them.

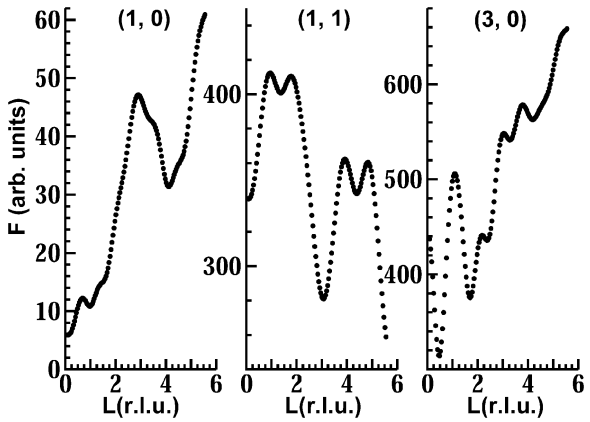

Fig. 4 Fractional order rods becoming the ($3\sqrt{3} \times 3\sqrt{3}$)*R*30° structure model of Fig. 1b.

$c(4 \times 2)$ structure largely dominates in stability the difference in γ with respect to the ($3\sqrt{3} \times 3\sqrt{3}$)*R*30° structure is much smaller for OT. The ($3\sqrt{3} \times 3\sqrt{3}$)*R*30° arrangement would allow a better optimization of vdW interactions for longer hydrocarbon chains than the $c(4 \times 2)$ staple lattice. In fact, we observe a decrease in ΔE_b in going from BT ($\Delta E_b = -0.34$ eV) to OT ($\Delta E_b = -0.30$ eV) as can be seen in Table 1. Taking into account that the ($3\sqrt{3} \times 3\sqrt{3}$)*R*30° lattice involves RS- species at the energetically unfavourable atop Au atom positions the decrease in ΔE_b with *n* can be entirely assigned to better organization of the alky

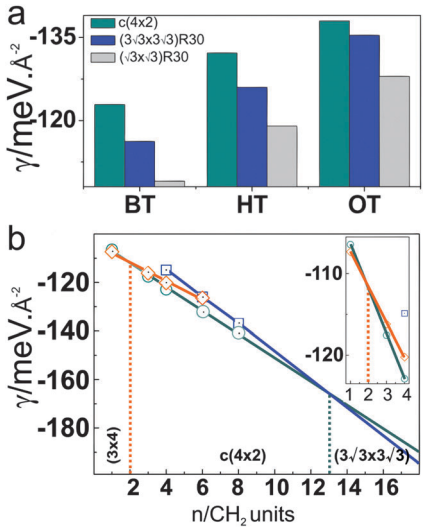

Fig. 5 (a) Bar chart of surface free energy (γ) corresponding to $c(4 \times 2)$ and ($3\sqrt{3} \times 3\sqrt{3}$)*R*30° lattices (with staples), and for the ($\sqrt{3} \times \sqrt{3}$)*R*30° on unreconstructed (U) Au(111) for BT, HT and OT. (b) Stability diagram for the $c(4 \times 2)$ and ($3\sqrt{3} \times 3\sqrt{3}$)*R*30° lattices as a function of the number of CH_2 units (*n*). The (3×4) to $c(4 \times 2)$ transition is also included (see details in the inset).

chains in this lattice (see Fig. 1). Also, we observe that accommodation of the longer alkyl chains for OT into the $c(4 \times 2)$ staple lattice forces the Au surface atoms in slightly more unfavourable positions, a fact which is reflected by an increase in the energy to reconstruct the metal surface (E_r) (Table 1).

Results in Fig. 5a could explain the increase in the ($\sqrt{3} \times \sqrt{3}$)*R*30°/$c(4 \times 2)$ ratio with *n*, and its decrease with temperature. The increasing influence of the vdW interactions among hydrocarbon chains on SAM organization is reflected in a decrease of α with *n* in agreement with broad-bandwidth sum frequency generation spectroscopy results.[45] One should expect that as the alkyl chains become longer the alkyl chain–Au interactions tend to vanish and the molecules become less tilted. This is not surprising, as crystalline monolayers of long hydrocarbon chains exhibit $0° < \alpha < 25°$.[46]

It is interesting to extrapolate the γ values for longer alkanethiolates than OT (Fig. 5b). The γ *vs.* *n* plot (Fig. 5b) shows that a transition of the $c(4 \times 2)$ to the ($3\sqrt{3} \times 3\sqrt{3}$)*R*30° structure would take place at $n > 13$, although the stability differences for $9 < n < 16$ are too small (<4 meV Å^{-2}) to be important and both lattices may be present. It is interesting to note that for DT[4] and HDT[5] SAMs on Au(111), where ($\sqrt{3} \times \sqrt{3}$)*R*30° predominates, a reasonable amount of $c(4 \times 2)$ (about 40%) is reached after annealing of the samples.[6]

We have included the (3×4) (staples in *trans* configuration) to $c(4 \times 2)$ (staples in *cis* configuration) phase transition observed for $n > 2$ (Fig. 5b inset), which is also driven by the vdW interactions, in order to have a complete phase diagram of alkanethiolates as a function of the hydrocarbon chain length.

Thus, for $1 < n < 13$ the adsorbed RS- radicals extract Au adatoms from the surface forming RS–Au_{ad}–SR moieties where the S electrons participate in bonding with the R group and

with two non-equivalent Au atoms (Au adatom in the complex and Au in the surface layer)[47] that allows a strong S–Au binding. For $n < 3$ these species organize in the (3×4) surface structure with the staples in *trans* configuration. For $n > 3$ the van der Waals interactions drive the system to the more stable $c(4 \times 2)$ surface structure with the staples in *cis* configuration.[22] For $n > 13$ the optimization of the vdW interactions favors $(3\sqrt{3} \times 3\sqrt{3})R30^\circ$ surface lattice over the $c(4 \times 2)$ lattice. Note that the (3×4), $c(4 \times 2)$ and $(3\sqrt{3} \times 3\sqrt{3})R30^\circ$ staple containing models are consistent with the experimentally observed vacancy islands coverage (0.12/0.14) at the Au terraces.[21,48]

Finally, it is important to discuss why the RS- species in the $(3\sqrt{3} \times 3\sqrt{3})R30^\circ$ lattice are adsorbed at the atop position rather than the fcc-bridge position preferred in the unreconstructed surface (Fig. 2, Table 2). In order to explain this point one should remember that alkanethiol physisorption is energetically favored in atop positions on the unreconstructed Au(111) surface.[49] We consider that after S–H bond scission the system chemisorbs and should evolve to the $c(4 \times 2)$ lattice for $n > 2$ and to the $(3\sqrt{3} \times 3\sqrt{3})R30^\circ$ lattice for $n > 13$ by extracting the corresponding amount of Au_{ad}, but with the S-heads remaining at the same top sites where physisorption takes place. Then, the single vacancies originated by this process can diffuse to nucleate and grow the vacancy islands observed by STM.

Conclusions

In conclusion, we show that a $(3\sqrt{3} \times 3\sqrt{3})R30^\circ$ model consisting of RS–Au_{ad}–SR moieties and RS- atop adsorbed species justifies most of the experimental data for the $(\sqrt{3} \times \sqrt{3})R30^\circ$ lattice. The new model proposed here explains both the $c(4 \times 2) \Leftrightarrow (\sqrt{3} \times \sqrt{3})R30^\circ$ reversible transitions, and the increase in the $(\sqrt{3} \times \sqrt{3})R30^\circ/c(4 \times 2)$ ratio as n is increased, providing a unified picture of the alkanethiol–Au(111) lattices in terms of RS–Au_{ad}–SR species.

Acknowledgements

The authors acknowledge financial support from ANPCyT (PICT 2554) and CONICET (PIP 00362), both from Argentina, and CTQ2011-24784 MICINN and MAT2012-38213-CO2-02 from Spain. P. C. thankfully acknowledges computer resources provided by Atlante, Canary Islands Supercomputing Infrastructure- Red Española de Supercomputación and the Computer Support Service for Research (SAII) at La Laguna University.

References

1 J. C. Love, L. A. Estroff, J. K. Kriebel, R. G. Nuzzo and G. M. Whitesides, *Chem. Rev.*, 2005, **105**, 1103–1169.
2 C. Vericat, M. E. Vela, G. Benitez, P. Carro and R. C. Salvarezza, *Chem. Soc. Rev.*, 2010, **39**, 1805–1834.
3 L. Tang, F. Li, W. Zhou and Q. Guo, *Surf. Sci.*, 2012, **606**, L31–L35.
4 P. Fenter, A. Eberhardt and P. Eisenberger, *Science*, 1994, **266**, 1216–1218.
5 X. Torrelles, E. Barrena, C. Munuera, J. Rius, S. Ferrer and C. Ocal, *Langmuir*, 2004, **20**, 9396–9402.
6 X. Torrelles, C. Vericat, M. E. Vela, M. H. Fonticelli, M. A. D. Millone, R. Felici, T. L. Lee, J. Zegenhagen, G. Munoz, J. A. Martin-Gago and R. C. Salvarezza, *J. Phys. Chem. B*, 2006, **110**, 5586–5594.
7 C. Vericat, G. Andreasen, M. E. Vela, H. Martin and R. C. Salvarezza, *J. Chem. Phys.*, 2001, **115**, 6672–6678.
8 G. E. Poirier and E. D. Pylant, *Science*, 1996, **272**, 1145–1148.
9 H. Gronbeck, H. Hakkinen and R. L. Whetten, *J. Phys. Chem. C*, 2008, **112**, 15940–15942.
10 O. Voznyy, J. J. Dubowski, J. T. Yates Jr. and P. Maksymovych, *J. Am. Chem. Soc.*, 2009, **131**, 12989–12993.
11 R. Mazzarello, A. Cossaro, A. Verdini, R. Rousseau, L. Casalis, M. F. Danisman, L. Floreano, S. Scandolo, A. Morgante and G. Scoles, *Phys. Rev. Lett.*, 2007, **98**, 016102.
12 A. Cossaro, R. Mazzarello, R. Rousseau, L. Casalis, A. Verdini, A. Kohlmeyer, L. Floreano, S. Scandolo, A. Morgante, M. L. Klein and G. Scoles, *Science*, 2008, **321**, 943–946.
13 P. D. Jadzinsky, G. Calero, C. J. Ackerson, D. A. Bushnell and R. D. Kornberg, *Science*, 2007, **318**, 430–433.
14 D.-e. Jiang, M. L. Tiago, W. Luo and S. Dai, *J. Am. Chem. Soc.*, 2008, **130**, 2777–2779.
15 Y. Li, G. Galli and F. Gygi, *ACS Nano*, 2008, **2**, 1896–1902.
16 M. A. MacDonald, P. Zhang, H. Qian and R. Jin, *J. Phys. Chem. Lett.*, 2010, **1**, 1821–1825.
17 H. Gronbeck and H. Hakkinen, *J. Phys. Chem. B*, 2007, **111**, 3325–3327.
18 H. Hakkinen, M. Walter and H. Gronbeck, *J. Phys. Chem. B*, 2006, **110**, 9927–9931.
19 D.-e. Jiang and S. Dai, *J. Phys. Chem. C*, 2009, **113**, 7838–7842.
20 M. Walter, J. Akola, O. Lopez-Acevedo, P. D. Jadzinsky, G. Calero, C. J. Ackerson, R. L. Whetten, H. Groenbeck and H. Hakkinen, *Proc. Natl. Acad. Sci. U. S. A.*, 2008, **105**, 9157–9162.
21 E. Pensa, E. Cortes, G. Corthey, P. Carro, C. Vericat, M. H. Fonticelli, G. Benitez, A. A. Rubert and R. C. Salvarezza, *Acc. Chem. Res.*, 2012, **45**, 1183–1192.
22 P. Carro, E. Pensa, C. Vericat and R. C. Salvarezza, *J. Phys. Chem. C*, 2013, **117**, 2160–2165.
23 J. Gao, F. Li and Q. Guo, *J. Phys. Chem. C*, 2013, **117**, 24985–24990.
24 L. Ferrighi, Y.-x. Pan, H. Gronbeck and B. Hammer, *J. Phys. Chem. C*, 2012, **116**, 7374–7379.
25 M. Yu, N. Bovet, C. J. Satterley, S. Bengió, K. R. J. Lovelock, P. K. Milligan, R. G. Jones, D. P. Woodruff and V. Dhanak, *Phys. Rev. Lett.*, 2006, **97**, 166102.
26 L. M. Molina and B. Hammer, *Chem. Phys. Lett.*, 2002, **360**, 264–271.
27 M. G. Roper, M. P. Skegg, C. J. Fisher, J. J. Lee, V. R. Dhanak, D. P. Woodruff and R. G. Jones, *Chem. Phys. Lett.*, 2004, **389**, 87–91.
28 M. Yu, N. Bovet, C. J. Satterley, S. Bengio, K. R. J. Lovelock, P. K. Milligan, R. G. Jones, D. P. Woodruff and V. Dhanak, *Phys. Rev. Lett.*, 2006, **97**, 166102.

29 G. Kresse and J. Hafner, *Phys. Rev. B: Condens. Matter Mater. Phys.*, 1993, **48**, 13115–13118.
30 G. Kresse and J. Furthmuller, *Comput. Mater. Sci.*, 1996, **6**, 15–50.
31 M. Dion, H. Rydberg, E. Schroder, D. C. Langreth and B. I. Lundqvist, *Phys. Rev. Lett.*, 2004, **92**, 246401.
32 J. Klimes, D. R. Bowler and A. Michaelides, *J. Phys.: Condens. Matter*, 2010, **22**, 074203.
33 P. E. Blochl, *Phys. Rev. B: Condens. Matter Mater. Phys.*, 1994, **50**, 17953–17979.
34 H. J. Monkhorst and J. D. Pack, *Phys. Rev. B: Condens. Matter Mater. Phys.*, 1976, **13**, 5188–5192.
35 W. B. Pearson, *Handbook of Lattice Spacing and Structure of Metals*, Pergamon Press, Inc., New York, 1958.
36 J. Tersoff and D. R. Hamann, *Phys. Rev. B: Condens. Matter Mater. Phys.*, 1985, **31**, 805–813.
37 E. Vlieg, *J. Appl. Crystallogr.*, 2000, **33**, 401–405.
38 D. Otalvaro, T. Veening and G. Brocks, *J. Phys. Chem. C*, 2012, **116**, 7826–7837.
39 D. Torres, P. Carro, R. C. Salvarezza and F. Illas, *Phys. Rev. Lett.*, 2006, **97**, 226103.
40 H. Kondoh, M. Iwasaki, T. Shimada, K. Amemiya, T. Yokoyama, T. Ohta, M. Shimomura and S. Kono, *Phys. Rev. Lett.*, 2003, **90**, 066102.
41 F. Li, L. Tang, W. Zhou and Q. Guo, *J. Am. Chem. Soc.*, 2010, **132**, 13059–13063.
42 A. Chaudhuri, T. J. Lerotholi, D. C. Jackson, D. P. Woodruff and V. Dhanak, *Phys. Rev. Lett.*, 2009, **102**, 126101.
43 A. Chaudhuri, T. J. Lerotholi, D. C. Jackson, D. P. Woodruff and V. R. Dhanak, *Surf. Sci.*, 2010, **604**, 227–234.
44 P. Carro, D. Torres, R. Diaz, R. C. Salvarezza and F. Illas, *J. Phys. Chem. Lett.*, 2012, **3**, 2159–2163.
45 N. Nishi, D. Hobara, M. Yamamoto and T. Kakiuchi, *J. Chem. Phys.*, 2003, **118**, 1904–1911.
46 B. M. Ocko, X. Z. Wu, E. B. Sirota, S. K. Sinha, O. Gang and M. Deutsch, *Phys. Rev. E: Stat. Phys., Plasmas, Fluids, Relat. Interdiscip. Top.*, 1997, **55**, 3164–3182.
47 H. Hakkinen, *Nat. Chem.*, 2012, **4**, 443–455.
48 N. A. Kautz and S. A. Kandel, *J. Phys. Chem. C*, 2009, **113**, 19286–19291.
49 Y. Yourdshahyan and A. M. Rappe, *J. Chem. Phys.*, 2002, **117**, 825–833.